Powder Technology 412 (2022) 118021

Contents lists available at ScienceDirect

Powder Technology

journal homepage: www.journals.elsevier.com/powder-technology

Implementation of real contact behaviour in the DEM modelling of triaxial tests on railway ballast

Mathias Tolomeo *, Glenn R. McDowell

Nottingham Centre for Geomechanics, University of Nottingham, Nottingham NG7 2RD, United Kingdom

HIGHLIGHTS

- Classic contact models do not work well for rough surfaces.
- Accounting for lower normal stiffness due to contact with asperities and plasticity.
- True contact behaviour implemented in numerical DEM simulations of ballast.
- Contact behaviour can explain small strain stiffness degradation.

GRAPHICAL ABSTRACT

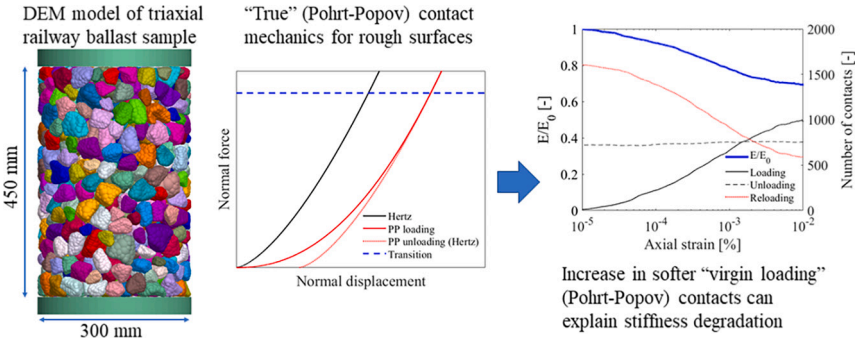

ARTICLE INFO

Keywords:
Contact mechanics
Discrete element method
Railway ballast
Triaxial test
Small strain stiffness

ABSTRACT

In the Discrete Element modelling of soils, the micromechanical behaviour at contacts has often been considered to have a minor influence on the macromechanical response, leaving basic theoretical models (e.g., Hertz) to describe the contact response in the normal direction. A realistic description of the contact response may be crucial especially when investigating small strain ranges. Recent experimental inter-particle loading tests on gravel suggest that the classic contact models fail to reproduce certain mechanical features, especially when roughness is significant. Here, some of these experimental observations, including a softer response than the Hertz model under loading in the normal direction, and plasticity on unloading, are implemented in a DEM model for the simulation of small strain tests on railway ballast. The influence of these features on small strain stiffness is highlighted. A micromechanical analysis is carried out to show how each of the contact-level features introduced affects the macroscopic response.

1. Introduction

It is well known that granular materials are complex systems for which the macroscopic behaviour is affected by a number of microscopic parameters. In the context of non-cohesive, frictional granular materials such as coarse-grained soils (sand and gravel), extensive research has aimed at showing the relation between the macroscopic and mesoscopic (fabric, including e.g. average particle and contact orientation and voids ratio) responses and microscopic quantities (shape of individual particles, interparticle friction). The relative density of a specimen is known

* Corresponding author.
E-mail address: mathias.tolomeo@nottingham.ac.uk (M. Tolomeo).

https://doi.org/10.1016/j.powtec.2022.118021
Received 11 August 2022; Received in revised form 7 October 2022; Accepted 10 October 2022
Available online 14 October 2022

to affect the peak shear strength and the volumetric behaviour; shape generally affects both peak and critical state strength [1], with angular particles offering a higher resistance because of the potential for interlocking; interparticle friction also affects the peak strength and, to a lower extent, the critical state strength, as shown both from experiments on spheres [2] and DEM simulations on different basic particle morphologies [3–5].

These established considerations have directed the research on the numerical modelling of soils with the Discrete Element Method (DEM). The main effort in the discrete modelling of tests on soils has been aimed at replicating the initial density (voids ratio) of an experimental sample and defining a realistic interparticle friction coefficient; only recently, the focus has extended to the modelling of real particle shape, which requires additional computational effort.

Contact mechanics, i.e., the modelling of the mechanical interaction between two grains when they are in contact, has often been omitted, except for the attention to the modelling of interparticle friction. Contact interactions in non-cohesive frictional soils are usually modelled by separating the response in the direction perpendicular to the contact plane (normal direction) from that along the contact plane (shear or tangential direction). Normal stiffness mostly affects the small strain response, whereas it has less effect on peak and critical state strength, and only little influence on the volumetric response at large shear strains [6]. Tangential forces become prevalent at larger strains, which is why the effort to reproduce realistic features of contact mechanics has generally been limited to capturing a realistic interparticle friction angle.

Contact stiffness can be of great relevance when the focus is on the small strain behaviour: in this case, both normal and tangential stiffnesses can significantly affect the macroscopic stiffness. This is particularly important in the initial phase in which contact topology remains unchanged and the global behaviour is essentially governed by contact deformation [7] rather than by geometrical rearrangements, although the influence of contact stiffness may also extend beyond this limit.

DEM has proven to be an excellent tool for the study of the behaviour at small strains, as it allows finer control of the application of deviatoric stress and can therefore provide stiffness measurement over a range of small strains that is usually difficult to access in static experimental tests [8].

In DEM, using a correct contact stiffness has the direct effect of influencing the small strain behaviour. It has though other indirect effects, e.g., it affects the number of contacts in a specimen: when a given confinement pressure is applied, different contact stiffnesses will generally result in a different number of contacts, even with little change in voids ratio, especially when real particle shape (particularly with concavity) is modelled and particles can touch each other at more than one contact point. This, in turn, may have an influence on the macroscopic response.

Recently, the need for a deeper understanding of contact behaviour has led to several experimental studies making use of specific interparticle loading devices, focusing at first on the measurement of interparticle friction [9] and normal and tangential behaviour [10] of sands, and eventually also on ballast [11]. These experimental observations show that the contact behaviour of real soil is complex, and the simple models usually employed in numerical simulations cannot capture some of its features. Roughness, in particular, can affect not just the tangential contact stiffness, but the normal stiffness too, especially at relatively low inter-particle loads, where the behaviour is often softer than predicted by the classic Hertz theory. This was also observed numerically by [12] using a combined discrete finite-element approach to model the contact between rough surfaces. Contact behaviour in the normal direction is also found to be not perfectly elastic, showing a stiffer response in unloading and reloading than first loading. Harkness et al. [13] modelled some form of damage at contact by introducing plasticity in the behaviour for the normal direction, assuming contact involves spherically capped conical asperities whose curvature (and therefore stiffness) can be modified if a yield stress is exceeded.

The aim of this paper is to take into account these experimental observations, and some recent attempts to define a more advanced contact model for the normal behaviour of ballast, by implementing a new contact law for DEM simulations of small strain stiffness probes of a large triaxial specimen of railway ballast, where real particle shape is also modelled using overlapping spheres (clumps).

DEM makes it possible to easily isolate the effect of multiple quantities on single aspects of the macroscopic response. In this case, small strain stiffness may be influenced by several factors, not limited to contact stiffness, such as fabric. In this paper, the effect of fabric will be separated from that of contact stiffness by replicating the same initial sample (and its fabric) and using it for tests with different contact models, so that the effect of the latter on the macroscopic response can clearly emerge for a given fabric.

2. Contact model

2.1. Normal direction: introducing roughness

At the state of the art, the vast majority of DEM applications on non-cohesive, frictional soils employ either a simple linear contact model (a spring with constant stiffness) or the classic elastic theory for the contact between smooth objects, resulting in the Hertz contact model [14], that introduces a pressure dependency in the behaviour, with the contact tangent stiffness being a function of the normal force ($k \propto F^{1/3}$). The Hertz model, however, typically fails to reproduce the macroscopic pressure dependency of small strain stiffness, as confirmed by many experimental findings, e.g., [15]. Goddard [16] proposes two independent mechanisms to explain the origin of these discrepancies: surface geometrical roughness, i.e. the presence of point-like contacts due to asperities when surfaces are not smooth, and particle rearrangements. Many researchers have focused on the former in the effort of modelling contact behaviour of soils to account for real features. Roughness gets immediately associated with the concept of friction, although the influence of roughness on the shearing behaviour is complex [11]; but it also affects the response in the normal direction, as contacts between rough surfaces will involve high-curvature asperities and occur at multiple contact points rather than cover a continuous surface, as is assumed in the classic elastic theory. Several contact models try to account for the effect of this reduced contact area on contact stiffness [17–22]. Generally, the proposed models give a lower normal stiffness than the Hertz stiffness for low forces, when contacts still involve asperities, followed by a transition to the Hertz behaviour at larger forces, when asperities get flattened and the contact involves a continuous area.

Recent experimental findings on the contact behaviour of a granite ballast [23], studied by means of the interparticle loading apparatus developed by [11], confirm this effect. Among the models proposed for contacts of rough surfaces, the Pohrt-Popov model [22] showed the best fit with the experimental data, that involved single contact particle-particle normal compression tests on ballast grains with several shapes (natural and sub-spherical) and surface morphologies (natural or polished). This was therefore chosen to model the contact response in the normal direction in the following DEM simulations.

The law proposed by Pohrt and Popov defines a new power law dependency of stiffness on the normal force ($k \propto F^{\alpha}$), where the exponent is a function of particle surface morphology (namely of the fractal dimension of the surface D_f). A threshold can be defined at the smallest value of normal force such that full contact happens, and this function only applies below such threshold, when contact still involves asperities; above the threshold, the behaviour can be assumed to follow the Hertz theory (Eq. (1) and Fig. 1):

Table 1
Input parameters used for the force-displacement laws in Fig. 1 with the Hertz and Pohrt-Popov model. Based on these input parameters, the area at full contact A_0 and the corresponding force $F_n(A_0)$ are determined from Eq. (5) and Eq. (4) as $A_0 = 6.68 \times 10^{-7}$ m^2 and $F_n(A_0) = 1775$ N, respectively.

Contact radius R^*	2.36 mm
Fractal dimension D_f	2.13
Root mean square height h	2.61×10^{-5} m
Young's modulus E	60 GPa
Poisson's ratio ν	0.25

$$k_{Pohrt-Popov} = \begin{cases} \frac{\pi}{10} D_f E^* \sqrt{A_0} \left(\frac{F}{hE^* \sqrt{A_0}} \right)^{0.2567\ D_f} & if\ F < F_{Hertz}(A_0) \\ k_{Hertz} = \left(6E^{*2} FR\right)^{1/3} & if\ F > F_{Hertz}(A_0) \end{cases} \quad (1)$$

where A_0 is the contact area when full contact happens, D_f and h are surface morphology parameters (fractal dimension and root mean square height, respectively) and E^* is the contact Young's modulus, derived from the Young's modulus E and Poisson's ratio ν of the material, as $1/E^* = 2(1-\nu^2)/E$. These are constants of the material; typical values for the Mount Sorrel granite ballast that was used in these experiments are $E = 60$ GPa [24] and $\nu = 0.25$.

When full contact happens, the force and stiffness of the two models are equal, and the contact area A_0 is the same as the contact area defined in the Hertz law:

$$A_0 = \pi \left(\frac{3FR}{4E^*} \right)^{2/3} \quad (2)$$

The corresponding stiffness is:

$$k_{Pohrt-Popov} = k_{Hertz} = 2E^* \sqrt{A_0/\pi} \quad (3)$$

and the transition force can be expressed as a function of the area A_0 based on the elastic theory:

$$(F_{Hertz})_{A_0} = \frac{4E^*}{3R} \left(\frac{A_0}{\pi} \right)^{3/2} \quad (4)$$

Replacing Eqs. (4) and (3) in Eq. (1), and solving for A_0, the following expression is obtained for the full contact area as a function only of known quantities of the contact (R, h, D_f):

$$A_0 = \frac{3}{4} \pi^{3/2} R\, h \left(\frac{20}{\pi^{3/2} D_f} \right)^{1/0.2567 D_f} \quad (5)$$

which, by substituting Eq. (5) in Eq. (1), allows an explicit definition of $k_{Pohrt-Popov}$ as a function only of contact force, particle surface parameters and contact geometry. The function is shown in Fig. 1, with $D_f = 2.13$ and $h = 2.61 \times 10^{-5}$ m obtained from the fitting of experimental data on the ballast employed; the Hertz law for the same set of parameters is also shown for comparison.

The numerical implementation of the contact law is carried out incrementally, i.e., at each time step a normal force increment is determined from the contact relative normal displacement δ_n and the stiffness $k_n = (k_n)_{F'}$, where F' is the force at the beginning of the time step. The magnitude of the normal force is then updated to $F = F' + k_n \delta_n$.

2.2. Normal direction: roughness and elasto-plasticity

Experimental data suggest that the behaviour in normal direction is far from elastic even at relatively small forces (~ tens of N). Upon unloading, data shows a stiffer response compared to virgin loading. When reloading on the same contact point, after having unloaded without losing contact, i.e. down to ~1 N, a similar stiffness as in the unloading branch is observed. Both branches are well fitted by the Hertz law. Therefore, in the simulations, a second, alternative law was also introduced, following the Pohrt-Popov equation under virgin loading and the Hertz equation under unloading and reloading; when the reloading curve reaches the maximum force experienced, it joins the curve for virgin loading (i.e. typically the Pohrt-Popov stiffness, unless forces are so high that the transition to full contact area with Hertz behaviour has occurred). This model, including plastic deformations and yielding, will be referred to as elasto-plastic Pohrt-Popov. An example is shown in Fig. 2.

Also in this case, the numerical implementation of the contact law is carried out incrementally, in the same way as described in the previous section, with an additional condition to limit the minimum force to zero and avoid tensile forces when unloading is complete ($F = 0$), so that tensile contacts do not occur if particles move apart. In addition to Eq. (1), the model is now defined also by the condition in Eq. (6), where F_{max} is the largest force experienced by the contact:

$$k_{Pohrt-Popov} = \begin{cases} \frac{\pi}{10} D_f E^* \sqrt{A_0} \left(\frac{F}{hE^* \sqrt{A_0}} \right)^{0.2567\ D_f} & if\ F = F_{max}\ and \Delta F > 0 \\ k_{Hertz} & if\ F < F_{max}\ or\ F = F_{max}\ and \Delta F < 0 \end{cases} \quad (6)$$

2.3. Tangential direction

The Pohrt-Popov model does not provide a theoretical framework for

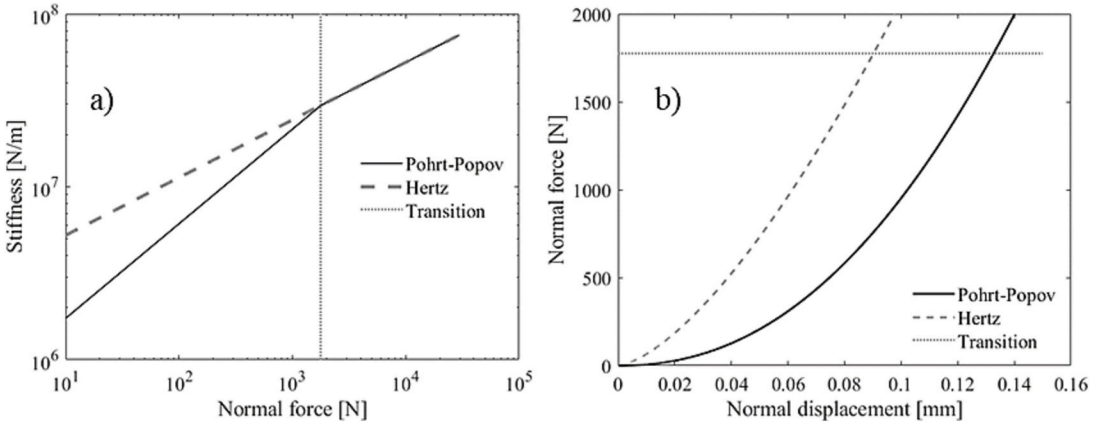

Fig. 1. a) Normal stiffness against normal force for the classic Hertz model and the rough surfaces Pohrt-Popov model. The parameters of the contact models are reported in Table 1. The dotted line shows the transition force $(F_n)_{A_0}$ above which the same (Hertz) stiffness is used for both models. b) Corresponding force-displacement curves.

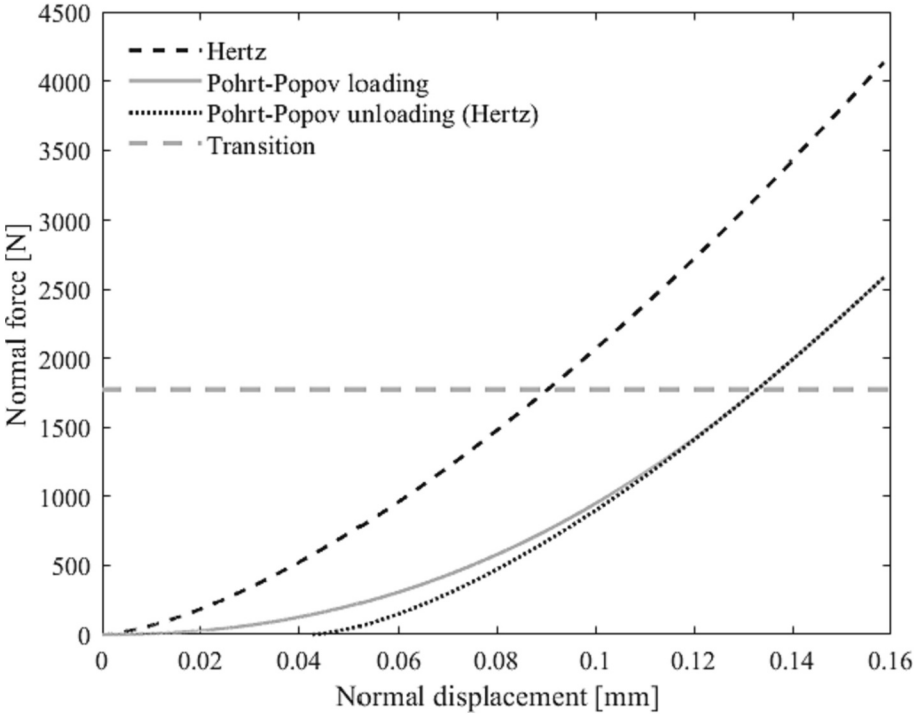

Fig. 2. Force-displacement curves for Hertz and Pohrt-Popov models, obtained with parameters defined in Table 1. The unloading branch of the modified elasto-plastic Pohrt-Popov model follows the Hertz stiffness.

the tangential stiffness, and the classic models (such as Mindlin-Deresiewicz) do not apply to the case of surfaces with topographic roughness, where contact involves asperities. Therefore, a simplified version of the Mindlin-Deresiewicz law was adopted, such that the ratio of tangential to normal stiffness k_r is assumed constant and equal to the ratio of the initial tangent of the force-displacement curve $k_s = 8G^*\sqrt{xR^*}$ to Hertz-Mindlin's normal stiffness $k_n = 2E^*\sqrt{xR^*}$, with x being the overlap:

$$\frac{k_s}{k_n} = k_r = \frac{2(1-\nu)}{2-\nu} \tag{7}$$

Preliminary experimental observations on single contact tests on ballast particles show that the actual tangential stiffness is often significantly lower than the stiffness predicted by any of the classic theories; however, in the absence of a model capturing this behaviour, it was decided to restrict the focus of this paper on the influence of the real contact mechanics in the normal direction.

The tangential law is complemented by the classic Coulomb condition that sets an upper limit to the magnitude of shear force, as a function of the magnitude of normal force, through the coefficient of interparticle friction. Experimental data on ballast [11] confirms that particles are generally characterised by a relatively high friction coefficient, that can vary as the contact is loaded, especially in the case of cyclic loading conditions; for simplicity, a constant value $\mu = 0.7$, which fits well the experimental data, is used here.

3. DEM model, sample preparation and loading conditions

In order to analyse the effect of different contact models, DEM simulations of small strain stiffness probes were performed, using the commercial software PFC3D [25]. The simulations reproduce the setup of typical laboratory tests on railway ballast carried out in the large triaxial device in use at the University of Nottingham [26]. Cylindrical specimens of ballast, with a diameter of 300 mm and a height of 450 mm, can be tested in this apparatus. Specimens are enclosed laterally by a flexible natural rubber membrane with 4 mm thickness, through which a constant lateral pressure is applied, and vertically by two stainless steel platens; after an isotropic confinement phase, deviatoric loading can be applied by moving upwards the lower ram and platen. A standardised, three steps vibro-compaction sample preparation procedure is found to consistently give a specimen with a voids ratio close to 0.700. The particle size distribution (PSD) follows the British Standards for railway ballast gradation [27] and can be found in Fig. 3.

In the simulations, the same voids ratio was targeted, although the preparation procedure was not replicated; particles were instead generated with random positions and orientations inside the cylindrical volume, following a size distribution scaled down from the target PSD, and then slowly expanded with no gravity until the target voids ratio was reached. This process was kept sufficiently slow so that the final sample would be stress-free.

Real particle shape was modelled through clumps, i.e., clusters of overlapping spheres filling the volume of a closed surface that describes the morphology of a particle [28]. The shapes modelled in these simulations come from a library of three different geometries that were obtained through 3D laser scans of ballast particles. The specimen was

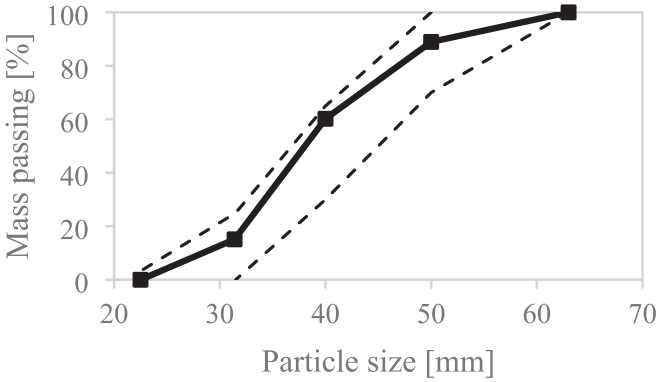

Fig. 3. Particle size distribution for the numerical specimen (solid line) and limits defined by the British Standards [27] (dashed lines).

generated with a total of 747 particles (Fig. 4), which were uniformly distributed in the three different shapes.

A good accuracy was sought in the reproduction of boundary conditions, i.e., the two stainless steel end platens and the lateral flexible membrane. End platens were modelled by two cylindrical disks with the platens' real dimensions and mass; their motion was restricted to vertical displacements. Rotation out of the horizontal plane was also allowed for the top platen, as for experiments where the platen can rotate about the contact point with the curved ram tip. A linear contact law was assumed for contacts between platens and grains, with an arbitrary stiffness $k_n = 3 \times 10^6$ N/m; such contacts were assumed to be frictionless, as end lubrication is generally adopted during laboratory tests in the large triaxial cell.

Modelling a flexible membrane in DEM can be a challenging task, but it becomes essential when such large particles (compared to the specimen size) are used, as in this case, and the lateral deformation of the sample is expected to be very heterogeneous, as the membrane follows the movement of particles and gets wrapped around them. To reproduce the flexibility of the membrane and allow a homogeneous application of the lateral pressure, a cylindrical layer of 12,600 bonded monodisperse spheres was used (Fig. 4), similar to several previous attempts [29–32]. The main properties are summarised in Table 2. In the initial configuration, spheres have a little overlap with their neighbours, to help avoid gaps; a lower density than that for natural rubber is therefore assigned to each sphere, to compensate for this effect as well as the excess thickness, so that the total mass matches the true membrane mass.

The tests that were simulated are small strain stiffness probes, with application of a deviatoric loading up to an axial strain of 0.1%, followed by unloading (Fig. 5). Before isotropic confinement, gravity is activated and the specimen is allowed to settle under its own (and the top platen's) weight, until equilibrium is reached. Isotropic confinement is then applied by slowly increasing the applied pressure until the target value $p = 150$ kPa is reached; the pressure is then kept constant until equilibrium is achieved.

An axial loading was then applied by imposing a vertical velocity to the bottom platen, while preventing the vertical motion of the top platen. In order to have accurate and smooth stiffness data in the range of small strains (here defined as the strains below 10^{-5}%), a very small velocity $v = 10^{-8}$ m/s was applied in the beginning of the probe. However, keeping this velocity for the whole probe would require an impractically long computational time; therefore, platen velocity was linearly increased in a range of deformation $\varepsilon_a = \Delta H/H_0 = 10^{-7}$ % ÷ 10^{-2}% until reaching a maximum value of 10^{-3} m/s to ensure the test remained quasi-static [33]. To verify this condition, so that inertial effects could be neglected, the inertial number $I = \dot{\varepsilon}\sqrt{m/\left(pd^{D-2}\right)}$ was calculated, where $\dot{\varepsilon}$ is the strain rate applied, m is the typical mass of a grain, $p = 150$ kPa the mean pressure, d the average grain diameter and D the dimension of the system. With the maximum platen velocity $v = 10^{-3}$ m/s, a value of $I \sim 10^{-5}$, largely below the limit of 10^{-3}, was obtained, therefore satisfying the quasi-static nature. Cundall's local damping was safely employed during both isotropic confinement and deviatoric loading to help the system reach equilibrium, given the quasi-staticity of the problem; the typical value of 0.7 was used for the damping coefficient α.

Table 2
Main parameters of the flexible membrane.

Number of spheres	12600
Membrane dimensions (height x internal diameter)	450 × 300 mm
Membrane normal bond stiffness	10^3 N/m
Membrane shear bond stiffness	–
Membrane bond strength	virtually unbreakable
Normal stiffness	10^6 N/m
Friction coefficient	0
Sphere density	248 kg/m^3
Sphere radius	5.4 mm

4. Results

4.1. Contact model including roughness

The implementation of experimental observations of contact behaviour started with the introduction of roughness, using the model presented in Section 2.1 and summarised by Eq. (1). To assess the effect

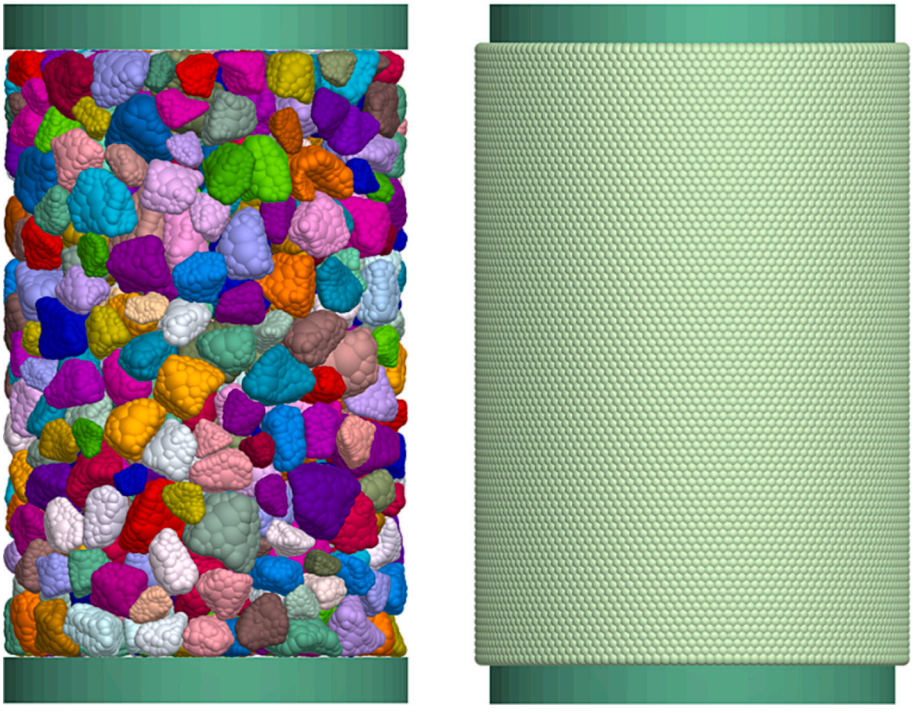

Fig. 4. Image of the triaxial sample with randomly colourised clumps to model particles (left) and bonded spheres to model the lateral flexible membrane (right).

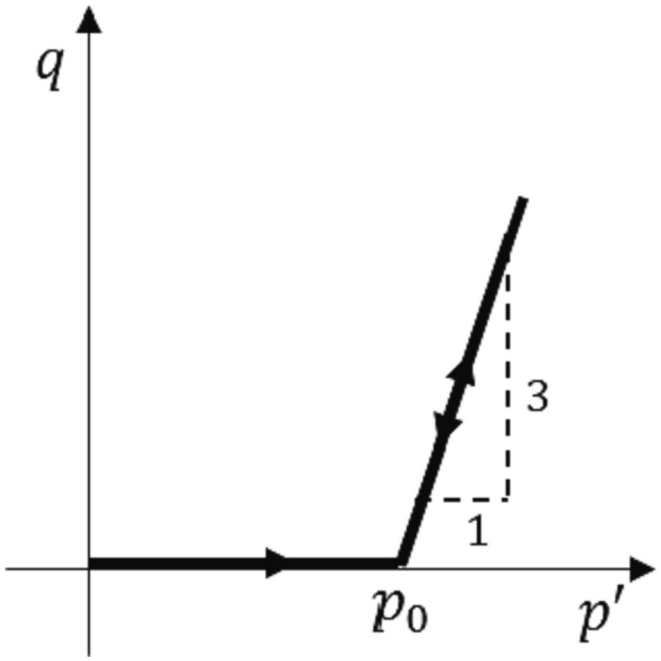

Fig. 5. Schematic representation of the stress path imposed in each probe, including a first phase of isotropic confinement up to a pressure $p_0 = 150$ kPa, an axial loading phase and a successive unloading.

of the new contact model, two simulations of small strain stiffness probes were carried out on the same original sample, one with the Hertz model and one with the Pohrt-Popov model, following the procedure detailed in Section 3; the macroscopic stiffness was calculated as the tangent Young's modulus in the vertical direction $E = \Delta\sigma_a/\Delta\varepsilon_a$, where $\Delta\varepsilon_a$ is the increment of axial deformation over one time step and $\Delta\sigma_a = \Delta q$ the corresponding increment of axial stress or deviatoric stress, with the lateral stress σ_r constant. All stress components were determined directly from contact forces, with the classic homogenisation expression $\sigma_{ij} = \frac{1}{V}\sum_{N_c} f_i l_j$ [34], where contact quantities $\vec{f}$ (contact force) and $\vec{l}$ (branch vector connecting the centroids of the two bodies in contact) are summed over all inter-particle contacts N_c lying inside volume V. The evolution of E with axial strain is shown in Fig. 6; a typical stiffness degradation curve for soils is shown for comparison in Fig. 7.

While sample preparation was identical for the two samples, the different contact model was responsible for a small difference in coordination number (number of contacts per particle) at the end of confinement: the generally softer contacts of the rough surface model caused a slightly higher coordination number compared to the Hertz case (5.6 to 5.3), which could potentially have some influence on the small strain stiffness (i.e., higher stiffness for higher number of contacts). Nevertheless, the small strain macroscopic stiffness for the Pohrt-Popov model was found to be sensibly lower than the one using the Hertz model, showing that the effect of contact stiffness prevailed with respect to a possible influence of the number of contacts. Despite the difference in coordination number, the average contact orientation at the end of confinement was similar between the two models, as verified by calculating the fabric tensor $\mathbf{F}$ defined from contact normal vectors $\mathbf{u}^c$ as in [35]:

$$\mathbf{G} = \frac{1}{N_c}\sum_{c=1}^{N_c} \mathbf{u}^c \otimes \mathbf{u}^c, \mathbf{F} = \frac{5}{2(1+e)}(3\mathbf{G} - \mathbf{I}) \tag{8}$$

where $c = 1, \ldots, N_c$ are all internal contacts in the sample, e is the voids ratio and $\mathbf{I}$ a 3×3 identity matrix. Some contact anisotropy, measured as the scalar norm of $\mathbf{F}$ ($F = \sqrt{\mathbf{F} : \mathbf{F}}$), was observed in both samples even under isotropic confinement, as the sample's and platen's own weights added a small amount of deviatoric stress; however, the amount of anisotropy ($F = 0.226$ and 0.228 for the Hertz and Pohrt-Popov test, respectively), and more generally the whole fabric tensor, were

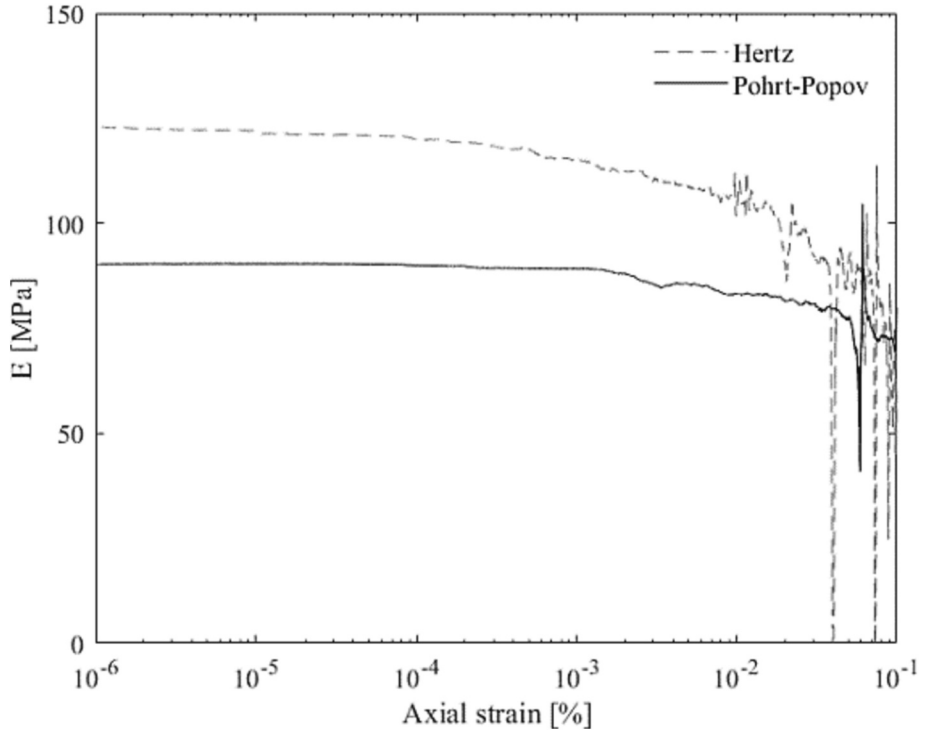

Fig. 6. Stiffness degradation curve for two simulations on the same initial sample using respectively the Hertz and Pohrt-Popov contact models for the normal direction. The macroscopic Young's modulus in the axial direction $E = \Delta\sigma_a/\Delta\varepsilon_a$ is shown, where $\Delta\varepsilon_a$ is an increment in axial strain and $\Delta\sigma_a$ the corresponding increment in axial stress.

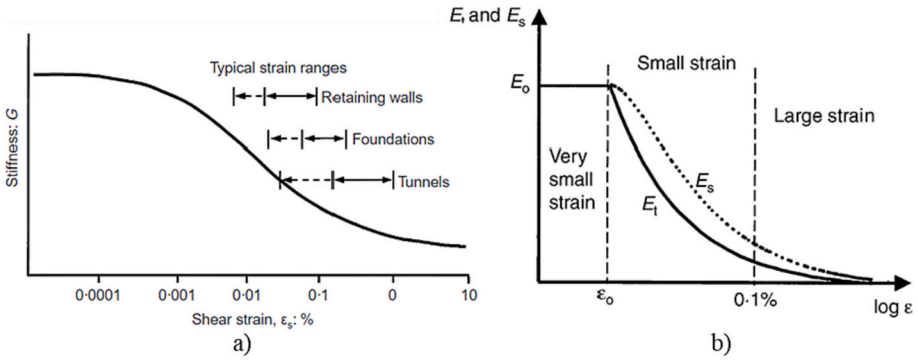

Fig. 7. a) Characteristic stiffness-strain behaviour of soil with typical strain ranges for structures [36,37]. b) Stiffness degradation of Young's modulus E, with E_t and E_s as the tangent and secant moduli respectively [38].

essentially identical between the two samples, which also shows that the excess in the number of contacts should not affect much the mechanical response to vertical loading.

Over the duration of the loading phase up to $\varepsilon_a = 0.1\%$, no contact was found to have exceeded the force at which stiffness transitions to the Hertzian one. This is typically quite large and is generally exceeded only by contacts in the main force chains under large strain deformations. It should also be noted that, for strains larger than $10^{-2}\%$, large oscillations appear in both stiffness curves; these are due to more intense particle rearrangement, whose effect on the macroscopic response tends to become predominant at this level of deformation with respect to the effect of contact stiffness.

4.2. Contact model including roughness and elasto-plasticity

Some plasticity was introduced to account for the stiffer contact behaviour during unloading and reloading observed in experiments, as described in Section 2.2. The behaviour on virgin loading, on the other hand, remained the same as in the previous example, following the Pohrt-Popov law. The complete law is defined in Eq. (6). It may seem that the macroscopic small strain stiffness should hardly be affected by this update of the model, given no change occurs for contacts undergoing virgin loading; however, comparing a probe with this modified model with the probe using the original (elastic) model as in Section 4.1, it becomes clear that simply accounting for this plasticity can significantly change the macroscopic stiffness even in the loading phase, as shown in Fig. 8. The small strain modulus E_0, here defined at an axial strain $\varepsilon_a = 10^{-5}\%$, was respectively 128 and 90 MPa in the two cases.

Fig. 8 also shows the degradation of the modulus for both simulations. While stiffness remains essentially constant over a quite large range of deformations for the elastic contact model, it starts degrading much earlier for the elasto-plastic case, with the two degradation curves approaching for deformations in the order of $10^{-2}\%$. The micromechanical origin for this behaviour can be searched in the evolution of the state of contacts, i.e., whether they are in virgin loading, unloading or reloading, how many of them are in each group, and how contacts in each group are oriented, which will now be explored.

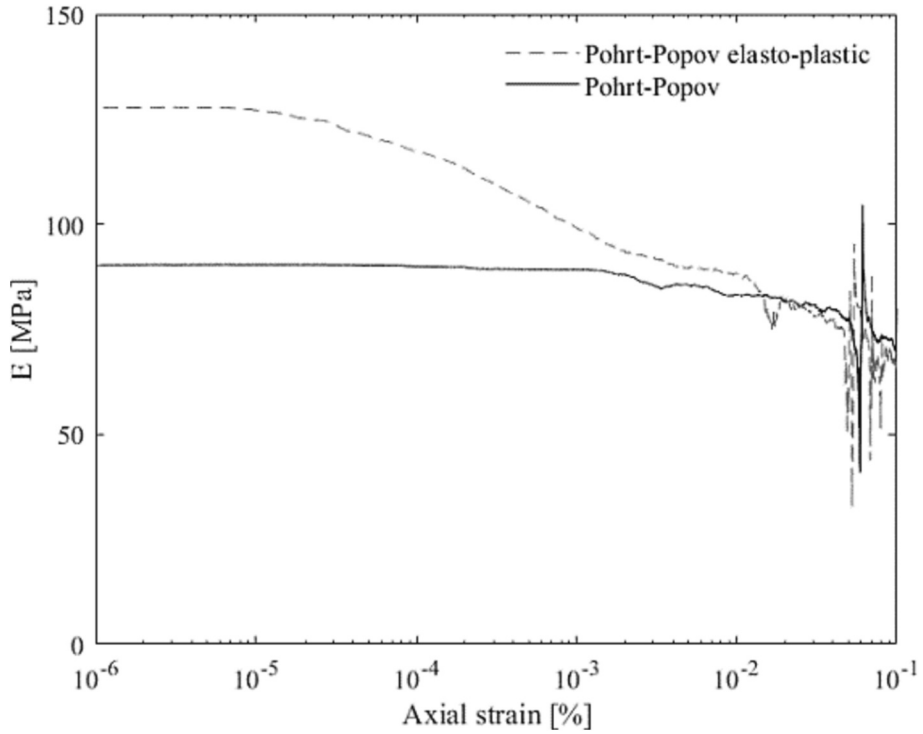

Fig. 8. Stiffness degradation curve for two simulations on the same initial sample using respectively the elasto-plastic (with stiffer, Hertz unloading/reloading) and elastic version of the Pohrt-Popov contact model for the normal direction. Only data from macroscopic loading is shown.

4.2.1. Micromechanical analysis

Fig. 9a shows the same stiffness degradation curve for the elasto-plastic case as in Fig. 8, together with the change in number of contacts for each contact state (virgin loading, unloading and reloading) and the total number of contacts. The data is only shown up to an axial strain $\varepsilon_a = 10^{-2}$%, since particle rearrangements occur beyond this point, and the correlation between micromechanical quantities and macroscopic response becomes less clear. Very few contacts are in virgin loading in the early stages of the probe, when most contacts appear to be reloading. This is because at the end of confinement most contacts are not exactly on their virgin loading curve; many of them will be close to it, but their current force might be smaller than the maximum force ever experienced, because of small oscillations while reaching equilibrium. When axial loading starts, such contacts will generally appear as reloading until they reach their maximum force and re-join the virgin loading curve. As this happens, the number of reloading contacts starts decreasing and at the same time the number of loading contacts starts increasing. This change starts at an axial strain close to 10^{-5}% which is in line with the start of stiffness degradation. Those contacts switching from reloading to loading state will change their stiffness, as they go from the stiffer Hertz law to the softer Pohrt-Popov law. The decrease in the number of reloading contacts follows very well the shape of the stiffness degradation curve, confirming that the change in contact stiffness is responsible for bulk stiffness degradation, and also that the initially higher modulus was caused by reloading contacts. The total number of contacts remains essentially unchanged, leaving the change in contact stiffness of individual contacts as the only explanation for stiffness degradation.

It can be interesting to look at the orientation of contacts in each group. To define a preferential orientation for the contacts in one group, a separate contact fabric tensor **F** was computed for each group (loading, unloading, reloading) based on Eq. (8), and its principal direction was determined as the eigenvector corresponding to the largest eigenvalue of the tensor. The angle between this eigenvector and the horizontal plane was then taken as a measure of the average orientation of contacts for each group, as shown in Fig. 9b.

Based on the external loading condition applied, contacts undergoing compression (loading and reloading contacts) are expected to align along the vertical direction. The orientation of contacts in the virgin loading group is close to 90°, corresponding to the vertical direction. Reloading contacts also show a vertical preferential orientation in the early stage of deformation; then, as more and more contacts shift to the loading group, those still reloading no longer show a clear preferential orientation. The average orientation of unloading contacts is close to the horizontal plane, where separation is most likely to occur, for the whole duration of the probe.

As previously mentioned, the state of a contact, and in particular the ratio of the current normal force to the largest force ever experienced, can be affected by the loading conditions. During confinement, as the confining pressure is gradually increased, normal forces at single contacts will also generally increase, reaching a steady value only after the target pressure is reached and then kept constant while the whole sample approaches equilibrium. The duration of the confinement phase can influence the state of single contacts: to show this, the test with elasto-plastic Pohrt-Popov model as in Fig. 9, for which the confining pressure had been gradually increased over 0.5 s, was repeated with slower confinement phases (respectively 4 and 10 times slower, Fig. 10a). With a slower confinement, while the number of contacts in each state (loading, unloading, reloading) at the start of the axial loading is essentially unchanged, the average ratio of current to maximum normal force for reloading contacts is slightly higher (0.89 for the original test and 0.90 and 0.93 respectively for the tests with 4 and 10 times slower confinement). The effect of this on the macroscopic behaviour is that the modulus starts degrading earlier (i.e., for smaller axial deformations) as the transition from reloading to virgin loading also starts earlier; apart from this difference, the behaviour is consistent both from a qualitative and a quantitative (essentially the same E_0 for the three tests) point of view. Fig. 10b compares stiffness degradation and evolution of the state of contacts for the case with slowest confinement (similarly to Fig. 9a), showing again a good correlation between stiffness degradation and change of contact state.

Even at small strains, the highly irreversible nature of deformations in granular materials clearly emerges when including the unloading phase of the probe (Fig. 5). A comparison of the two contact models (Fig. 11a) shows that higher unloading stiffness when using the elasto-plastic model is associated with larger plastic deformations. Similarly to the loading phase, for unloading the origin of this difference in macroscopic stiffness can be attributed to the difference in contact stiffness: with the elasto-plastic model, as soon as the direction of the macroscopic loading is inverted, most vertical contacts that were in virgin loading will immediately undergo unloading, with a consequent increase in contact stiffness. In contrast to the loading phase, where the amount of reloading contacts in the vertical direction (responsible for the higher stiffness) starts degrading early, here it is the unloading contacts in the vertical direction that are responsible for higher stiffness, and these will remain in this state for the whole duration of macroscopic unloading. Therefore, the effect on macroscopic stiffness will last for longer, as shown in Fig. 11b. The number of contacts in each state and their preferential orientations during the unloading phase are shown in Fig. 12a-b, confirming that the number of contacts (mostly vertical)

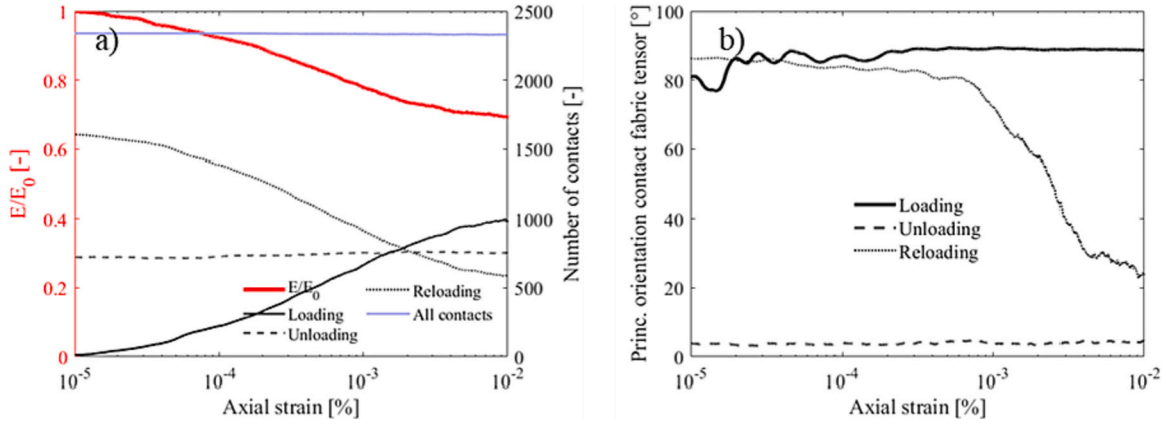

Fig. 9. a) Stiffness degradation curve for the elasto-plastic Pohrt-Popov model, normalised by the modulus E_0 at $\varepsilon_a = 10^{-5}$%. The evolution of the number of contacts in each state for the normal direction (virgin loading, unloading, reloading) and the total number of contacts are also shown, with scale on the right axis. Only data from the loading part of the probe is shown. b) Evolution of the angle between the principal orientation of the contact fabric tensor and the horizontal plane, for the same groups of contacts as in the left figure.

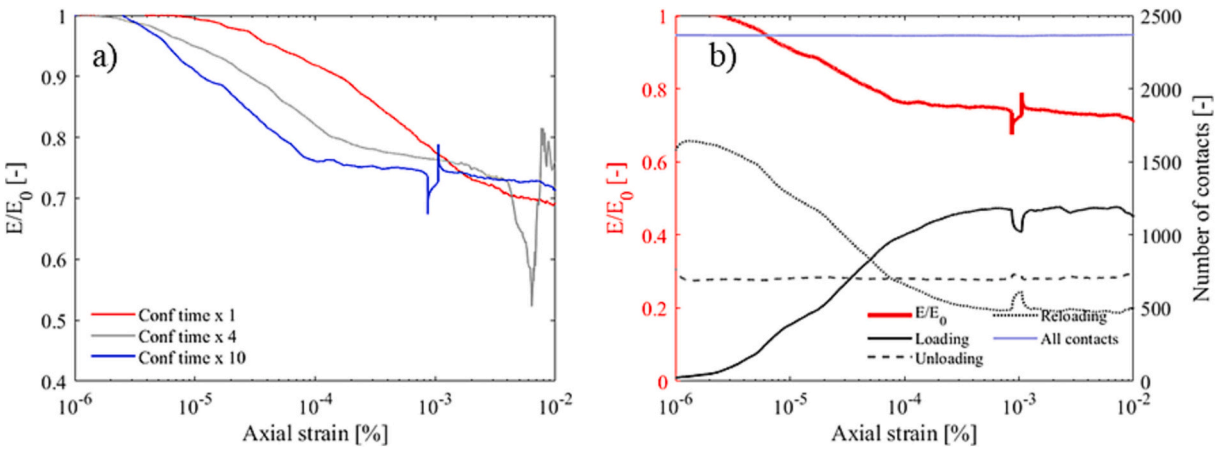

Fig. 10. a) Stiffness degradation curves for the elasto-plastic Pohrt-Popov model (red curve, same as in Fig. 9a) and for two more tests with the same model and sample but slower confinement phases (respectively 4 and 10 times slower). E_0 values are 128, 131 and 130 MPa respectively. b) Stiffness degradation curve for the test with slowest confinement with evolution of the number of contacts in each state for the normal direction. (For interpretation of the references to colour in this figure legend, the reader is referred to the web version of this article.)

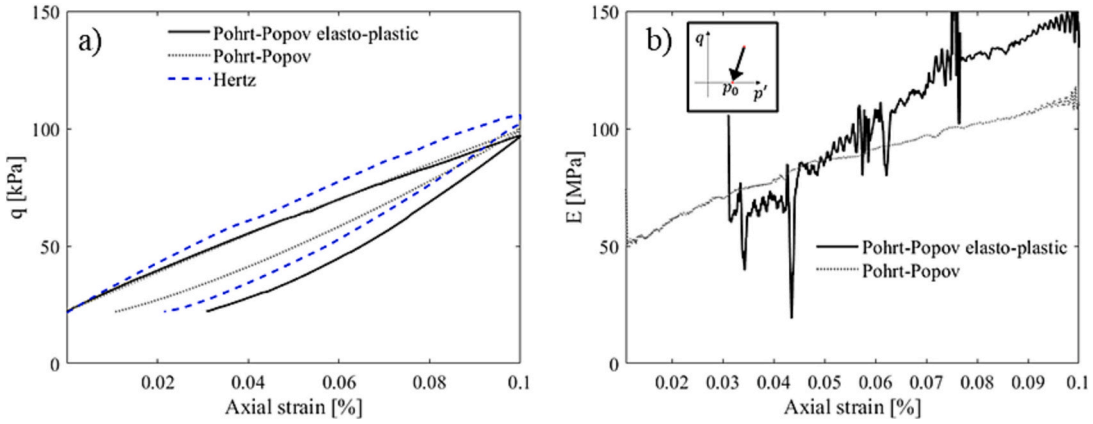

Fig. 11. a) Deviatoric stress against axial strain for the original (elastic) and modified (elasto-plastic) Pohrt-Popov model. The Hertz case is also shown for comparison. Both macroscopic loading up to $\varepsilon_a = 0.1\%$ and macroscopic unloading down to $q = q_0$ are shown. It should be noted that at the start of the probe the deviatoric stress q is larger than zero due to the sample's and top platen's own weight. b) Stiffness in the macroscopic unloading phase for the original (elastic) and modified (elasto-plastic) Pohrt-Popov model. The inset shows a sketch of the unloading stress path applied.

undergoing virgin loading during the first phase, which was still significant towards the end of the loading phase (Fig. 9a), drops as soon as the load direction changes, whereas unloading contacts, that used to be aligned in the horizontal plane, are now mainly vertical, essentially replacing those virgin loading contacts. Unloading contacts then remain mostly vertical for the whole duration of this phase. Some of the

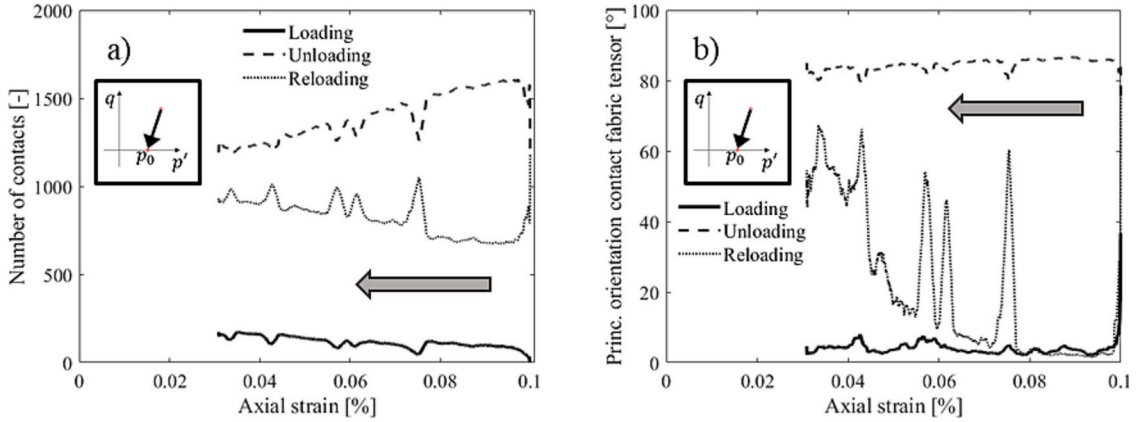

Fig. 12. a) Number of contacts in each state (loading, unloading, reloading) for the elasto-plastic Pohrt-Popov model during the unloading phase of the probe. b) Evolution of the angle between the principal orientation of the contact fabric tensor and the horizontal, during the unloading phase of the probe, for the same groups of contacts as in the left figure. The two insets show a sketch of the unloading stress path applied.

unloading contacts eventually separate (i.e., zero force), which explains the small decrease in their number; however, they remain the predominant group for the whole duration of the unloading phase. The relatively few contacts undergoing virgin loading now lie close to the horizontal plane. Reloading contacts show a preferential horizontal orientation in the beginning of unloading, similarly to virgin loading contacts, but then become more scattered, showing a less clear trend, as particle rearrangement intensifies.

5. Conclusions

Experimental observations on contact mechanics between railway ballast particles were implemented in a DEM model by means of a contact law for rough surfaces and applied to the simulation of small strain stiffness probes on ballast in a large triaxial cell, for which real shape was also modelled. Preliminary results show a significant change in small strain stiffness, that can be attributed to the different contact normal stiffness between the rough surface model and the classic Hertz model. Plasticity was also implemented to account for the experimental stiffer response on unloading and reloading; this surprisingly showed a significant influence on the response in the macroscopic loading phase, as well as in the unloading phase. Micromechanical observations of the behaviour of single contacts during each phase have explained the macroscopic observations, giving a rational explanation of the degradation of modulus in the small strain region: it is the increase in the number of virgin contacts as the contact force exceeds its maximum previous value and the contact stiffness transitions from the stiffer Hertz value to the softer Pohrt-Popov one for rough particles. All these results show the importance of a correct description of contact mechanics features when creating a DEM model of a coarse-grained soil. This is part of the effort towards more physically based DEM simulations that may complement, and eventually replace, standard laboratory tests, particularly for materials such as railway ballast for which experimental tests can be impractical.

While the focus of this work was restricted to the comparison of different contact models in numerical simulations, in the future a comparison with experimental data will be needed, not just from a quantitative point of view (e.g., to determine small strain stiffness moduli) but also from a qualitative one (e.g., focusing on the shape of the stiffness degradation curve). For a quantitative comparison, a more realistic geometrical description of a laboratory sample is needed, including measurement of all particle shapes, positions and orientations (i.e. fabric), to finally create a numerical “avatar” of a laboratory specimen.

In addition, further refinements of the contact behaviour may be considered in the future, to include other experimental observations and build a more advanced contact model. This may include contact damage under normal force, so that a softer response occurs under high loads as local breakage occurs, before bulk breakage of the particle. Other forms of damage could be considered, such as abrasion, that can have both a mechanical effect (e.g., change of interparticle friction) and a geometrical effect (e.g., flattening of asperities, as already modelled in DEM by [39]). The response in the tangential direction also needs further understanding and a better description, to account for preliminary experimental observations showing a much lower stiffness than the stiffness predicted by any of the classic theories.

CRediT authorship contribution statement

Mathias Tolomeo: Conceptualization, Methodology, Software, Investigation, Data curation, Writing – original draft. **Glenn R. McDowell:** Conceptualization, Methodology, Resources, Writing – review & editing, Supervision, Project administration, Funding acquisition.

Declaration of Competing Interest

The authors declare that they have no known competing financial interests or personal relationships that could have appeared to influence the work reported in this paper.

Data availability

Data will be made available on request.

Acknowledgments

This work was supported by the Engineering and Physical Sciences Research Council [grant number EP/S026460/1] in collaboration with Professor M. R. Coop and Dr. B. A. Baudet at University College London and Dr. A. Zervos at University of Southampton. This work follows the experimental work carried out at University College London by Dr. F. Altuhafi, whose contribution in the development of the contact law used here is acknowledged.

References

[1] G.-C. Cho, J. Dodds, J.C. Santamarina, Particle shape effects on packing density, stiffness, and strength: natural and crushed sands, J. Geotech. Geoenviron. Eng. 132 (5) (2006) 591–602.
[2] A.E. Skinner, A note on the influence of interparticle friction on the shearing strength of a random assembly of spherical particles, Geotechnique 19 (1) (1969) 150–157.
[3] J. Gong, J. Zou, L. Zhao, L. Li, Z. Nie, New insights into the effect of interparticle friction on the critical state friction angle of granular materials, Comput. Geotech. 113 (March) (2019) 103105.
[4] A.A. Peña, A. Lizcano, F. Alonso-Marroquin, H.J. Herrmann, Biaxial test simulations using a packing of polygonal particles, Int. J. Numer. Anal. Methods Geomech. 32 (2) (Feb. 2008) 143–160.
[5] T. Binaree, E. Azéma, N. Estrada, M. Renouf, I. Preechawuttipong, Combined effects of contact friction and particle shape on strength properties and microstructure of sheared granular media, Phys. Rev. E 102 (2) (2020) 22901.
[6] F. Radjai, F. Dubois, Modélisation numérique discrète des matériaux granulaires, 2010.
[7] J.-N. Roux, The nature of quasistatic deformation in granular materials, in: Powders Grains 2005 - Proc. 5th Int. Conf. Micromechanics Granul. Media vol. 1, 2005, pp. 261–265.
[8] N.S.C. Reddy, H. He, K. Senetakis, DEM analysis of small and small-to-medium strain shear modulus of sands, Comput. Geotech. 141 (October 2021) (2022) 104518.
[9] K. Senetakis, M.R. Coop, M.C. Todisco, The inter-particle coefficient of friction at the contacts of Leighton Buzzard sand quartz minerals, Soils Found. 53 (5) (2013) 746–755.
[10] V. Nardelli, M.R. Coop, The experimental contact behaviour of natural sands: Normal and tangential loading, Geotechnique 69 (8) (2019) 672–686.
[11] C.P.Y. Wong, M.R. Coop, Development of inter-particle friction in a railway ballast, Geotech. Lett. 10 (4) (2020) 535–541.
[12] S. Nadimi, M. Otsubo, J. Fonseca, C. O'Sullivan, Numerical modelling of rough particle contacts subject to normal and tangential loading, Granul. Matter 21 (4) (2019) 1–14.
[13] J. Harkness, A. Zervos, L. Le Pen, S. Aingaran, W. Powrie, Discrete element simulation of railway ballast: modelling cell pressure effects in triaxial tests, Granul. Matter 18 (3) (Aug. 2016) 65.
[14] R.D. Mindlin, H. Deresiewicz, Elastic spheres in contact under varying oblique forces, J. Appl. Mech. 20 (3) (Jun. 1953) 327–344.
[15] B.O. Hardin, F.E. Richart, Elastic wave velocities in granular soils, J. Soil Mech. Found. Div. 89 (1) (Feb. 1963) 33–65.
[16] J.D. Goddard, Nonlinear elasticity and pressure-dependent wave speeds in granular media, Proc. R. Soc. London. Ser. A Math. Phys. Sci. 430 (1878) (1990) 105–131.
[17] J.A. Greenwood, J.B.P. Williamson, F.P. Bowden, Contact of nominally flat surfaces, Proc. R. Soc. Lond. Ser. A. Math. Phys. Sci. 295 (1442) (Dec. 1966) 300–319.
[18] J.A. Greenwood, J.H. Tripp, The elastic contact of rough spheres, J. Appl. Mech. 34 (1) (Mar. 1967) 153–159.
[19] J.A. Greenwood, K.L. Johnson, E. Matsubara, A surface roughness parameter in Hertz contact, Wear 100 (1) (1984) 47–57.
[20] S. Yimsiri, K. Soga, Micromechanics-based stress-strain behaviour of soils at small strains, Geotechnique 50 (5) (2000) 559–571.
[21] M. Bahrami, M.M. Yovanovich, J.R. Culham, A compact model for spherical rough contacts, J. Tribol. 127 (4) (Apr. 2005) 884–889.
[22] R. Pohrt, V.L. Popov, Normal contact stiffness of elastic solids with fractal rough surfaces, Phys. Rev. Lett. 108 (10) (2012) 1–4.
[23] F. Altuhafi, B. Baudet, M.R. Coop, An Investigation of the Applicability of Contact Models to the Normal Load-Deflection Behaviour of Artificially Shaped Granite (Under review), 2022.
[24] A.A. Afrouz, Practical Handbook of Rock Mass Classification Systems and Modes of Ground Failure, CRC Press, 1992.

[25] PFC — Particle Flow Code, Ver. 7.0, Itasca Consulting Group, Inc, Minneapolis: Itasca, 2021.
[26] B. Aursudkij, G.R. McDowell, A.C. Collop, Cyclic loading of railway ballast under triaxial conditions and in a railway test facility, Granul. Matter 11 (6) (2009) 391–401.
[27] EN 13450, B, Aggregates for Railway Ballast, British Standards Institution, 2013.
[28] R. Taghavi, Automatic clump generation based on mid-surface, in: The 2nd International FLAC/DEM Symposium, 2011, pp. 791–797, no. June.
[29] J. Zhang, X. Wang, Z.Y. Yin, Z. Liang, DEM modeling of large-scale triaxial test of rock clasts considering realistic particle shapes and flexible membrane boundary, Eng. Geol. 279 (October) (2020) 105871.
[30] R. Kawamoto, E. Andò, G. Viggiani, J.E. Andrade, All you need is shape: predicting shear banding in sand with LS-DEM, J. Mech. Phys. Solids 111 (2018) 375–392.
[31] J. de Bono, G.R. McDowell, D. Wanatowski, Discrete element modelling of a flexible membrane for triaxial testing of granular material at high pressures, Geotech. Lett. 2 (4–6) (2012) 199–203.
[32] M.B. Cil, K.A. Alshibli, 3D analysis of kinematic behavior of granular materials in triaxial testing using DEM with flexible membrane boundary, Acta Geotech. 9 (2) (2014) 287–298.
[33] G. Midi, On dense granular flows, Eur. Phys. J. E 14 (4) (2004) 341–365.
[34] J. Christoffersen, M.M. Mehrabadi, S. Nemat-Nasser, A micromechanical description of granular material behavior, J. Appl. Mech. 48 (2) (1981) 339.
[35] C.F. Zhao, G. Pinzón, M. Wiebicke, E. Andò, N.P. Kruyt, G. Viggiani, Evolution of fabric anisotropy of granular soils: x-ray tomography measurements and theoretical modelling, Comput. Geotech. 133 (March) (2021).
[36] J.H. Atkinson, G. Sallfors, Experimental determination of soil properties, in: Proceedings of the 10th ECSMFE vol. 3, 1991, pp. 915–956.
[37] R. Mair, Developments in geotechnical engineering research: applications to tunnels and deep excavations. Unwin memorial lecture 1992, in: Proc. Instn Civ. Engrs Civ. Engng vol. 3, 1993, pp. 27–41.
[38] J.H. Atkinson, Non-linear soil stiffness in routine design, Geotechnique 50 (5) (2000) 487–508.
[39] J. de Bono, H. Li, G.R. McDowell, A new abrasive wear model for railway ballast, Soils Found. 60 (3) (2020) 714–721.